

## A Practical Scheme for Calculating the Fire-Induced Winds in the October 20, 1991 Oakland Hills Fire

J. Trelles & P.J. Pagni

Mechanical Engineering Department

University of California, Berkeley, CA USA 94720

### Problem Statement

This research is based on the model developed by Howard Baum and Bernard McCaffrey [1]. As a first step, a consistent set of characteristic scales are chosen to nondimensionalize all physical parameters and variables. The greatest advantage obtained by the following choice of nondimensionalization is that, once one has solved for the flow field induced by a single fire, the field produced by a series of fires is given by physically scaling each fire and then vectorially adding all the influences at a point. The nominal heat release,  $Q_o$ , the ambient density,  $\rho_o$ , the ambient temperature,  $T_o$ , the specific heat,  $c_p$ , and the acceleration of gravity,  $g$ , are used to determine characteristic quantities, which are subscripted with a "c". The expressions for the characteristic length,  $L$ , velocity,  $U$ , vorticity,  $\omega$ , potential,  $\Phi$ , and Stokes stream function,  $\Psi$ , are given in Eq. (1). All the subsequent nondimensional quantities - superscripted with an asterick - are obtained by dividing the dimensional quantity by the characteristic quantity.

$$L_c = \left( \frac{Q_o}{\rho_o c_p T_o \sqrt{g}} \right)^{2/5} \quad U_c = \left( \frac{g^2 Q_o}{\rho_o c_p T_o} \right)^{1/5} \quad \omega_c = \left( \frac{g^3 \rho_o c_p T_o}{Q_o} \right)^{1/5} \quad (1)$$

$$\Phi_c = \left( \frac{g^{1/3} Q_o}{\rho_o c_p T_o} \right)^{3/5} \quad \Psi_c = \frac{Q_o}{\rho_o c_p T_o}$$

The detailed fluid mechanics are approached by using the technique of flow field decomposition [1]. The nondimensional flow field,  $\mathbf{u}^*$ , is described in axisymmetric cylindrical coordinates (see Fig. 1) by the summation of an irrotational expansion velocity,  $\mathbf{w}^*$ , governed by a potential,  $\Phi^*(r^*, z^*)$ , and a vorticity driven solenoidal velocity,  $\mathbf{v}^*$ , described by a stream function,  $\Psi^*(r^*, z^*)$ , as shown in Eqs. (2 and 3).

$$u_r^* = \frac{\partial \Phi^*}{\partial r^*} - \frac{1}{r^*} \frac{\partial \Psi^*}{\partial z^*} \quad u_z^* = \frac{\partial \Phi^*}{\partial z^*} + \frac{1}{r^*} \frac{\partial \Psi^*}{\partial r^*} \quad (2, 3)$$

This technique incorporates the time-averaged, empirically determined Gaussian profiles [2] for vertical velocity,  $u_o$ , and temperature,  $T$ ,

$$u_o = U_m(z) \exp \left\{ - \left( \frac{r}{R(z)} \right)^2 \right\}, \quad \frac{(T - T_o)}{T_o} = \Theta(z) \exp \left\{ - \left( \frac{r}{\lambda R(z)} \right)^2 \right\}. \quad (4)$$

$R(z)$  is the 1/e width of the Gaussian profile.  $\lambda$  is the ratio of the thermal to the momentum width.  $U_m(z)$  and  $\Theta(z)$  are the averaged empirical centerline values which have the form  $U_m(z^*) = A(z^*)^n$  and  $\Theta(z^*) = B(z^*)^{2n-1}$ .  $A$ ,  $B$ , and  $n$  depend on the vertical flame region. For completeness, a fit for the width,  $R_f^*(z^*) = C + D(z^*)^{3(1-2n)/5}$ , based on the results of Eq. (10) is included.

TABLE I. Plume Correlation Parameters

Region	Range	n	A	B	C	D
Flame	$0 < z^* < 1.32$	1/2	2.18	2.91	0	0.417
Intermittent	$1.32 < z^* < 3.3$	0	2.45	3.81	0.255	0.137
Plume	$z^* > 3.3$	-1/3	3.64	8.41	0.136	0.121

McCaffrey's data [2] suggests that  $\lambda = 0.75^{1/2} = 0.866$  is acceptable. This value is used in this analysis to permit comparisons with Ref. [1]. The time averaged convective energy flux  $H(z)$  is defined and expressed in terms of the parameters in Eqs. (4) as

$$H(z) = 2\pi c_p \int_0^\infty \rho u_e (T - T_o) r dr = 2\pi c_p \Theta(z) U_m(z) \int_0^\infty \rho \exp\left\{-\left(\frac{r}{\lambda R(z)}\right)^2 (1 + \lambda^2)\right\} r dr. \quad (5)$$

Using the equation of state  $\rho T = \rho_o T_o$  and the second of Eqs. (4) to eliminate  $\rho$  in Eq. (5) gives

$$H(z) = 2\pi c_p \rho_o T_o \Theta(z) U_m(z) \int_0^\infty \exp\left\{-\left(\frac{r}{R(z)}\right)^2\right\} \left[1 - \frac{1}{1 + \Theta(z) \exp\left\{-\left(\frac{r}{\lambda R(z)}\right)^2\right\}}\right] r dr. \quad (6)$$

Defining  $i_\lambda(\Theta^*(z^*))$  as the integral in Eq. (6) and applying the transformations

$$t = e^{-(r/R)^2}, \quad r dr = -\frac{1}{2} R^2 e^{(r/R)^2} dt, \quad (7)$$

yields

$$i_\lambda(\Theta(z)) = \frac{1}{2} R^2 \left[1 - \int_0^1 \frac{dt}{\{1 + [\Theta^*(z^*)] [t^{1/\lambda^2}]\}}\right] = \frac{1}{2} R^2 [1 - I_\lambda(\Theta^*(z^*))]. \quad (8)$$

Defining  $I_\lambda(\Theta^*(z^*))$  as the integral in Eq. (8) and inserting Eq. (8) into Eq. (6) yields the convective energy flux  $H(z)$ . By using the characteristic lengths in Eqs. (1), one obtains an  $H^*(z^*)$  that is nondimensionalized on  $Q_o$ .

$$H^*(z^*) = \frac{H(z)}{Q_o} = \frac{\pi c_p \rho_o T_o U_m(z) R^2(z)}{Q_o} [1 - I_\lambda(\Theta^*(z^*))] = \pi U_m^*(z^*) R^{*2}(z^*) [1 - I_\lambda(\Theta^*(z^*))] \quad (9)$$

In the plume region,  $H^*(z^*) = (1 - \chi)$ , i.e., a constant, where  $\chi$  is the fraction of the heat that is radiated away. There Eq. (9) can be solved for  $R^*(z^*)$ ,

$$R^*(z^*) = \sqrt{\frac{1 - \chi}{\pi U_m^*(z^*) [1 - I_\lambda(\Theta^*(z^*))]}}. \quad (10)$$

Baum and McCaffrey [1] show that this expression for  $R^*(z^*)$  holds throughout the intermittent and plume regions. For the continuous flame region, the width is nearly constant,  $R^*(z^*) \approx R_o^*(1.32) = 0.417$ . Figure 2 shows  $I_\lambda(\Theta^*(z^*))$ ,  $R^*(z^*)$ , and the fit for  $R^*(z^*)$  from Table I.  $I_\lambda$  is numerically determined using the Romberg quadrature routine *qromb* detailed in Ref. [3] for  $\lambda = 0.866$ . The accuracy of this technique is verified by calculating  $I_\lambda$  for  $\lambda = 1$  and comparing with the exact logarithmic answer. For  $z^* > 20$ , asymptotic expressions for  $I_\lambda$  and  $R^*$  may be used. Throughout the text, all asymptotic quantities are subscripted with an "a". Assuming  $\Theta^* \ll 1$  in Eq. (8) gives

$$I_{\lambda a}(\Theta^*(z^*)) = 1 - \frac{B}{1 + 1/\lambda^2} (z^*)^{-5/3} \quad (11)$$

which yields from Eq. (10),

$$R_a^*(z^*) = \sqrt{\frac{(1 - \chi) (1 + 1/\lambda^2)}{\pi A B}} z^*. \quad (12)$$

For  $\chi = 0.35$ ,  $R_a^*(z^*) = 0.13z^*$  which verifies that the plume produced by a fire of finite volume approaches the point source plume in the large  $z^*$  limit.  $R_a^*(z^*)$  should be used for  $z^* > 20$ . Thus, Eqs. (4, 10, and 12) and Table I define the empirical vertical velocity and temperature fields. To obtain the radial velocities, the following analyses are made.

### Potential for Expansion Velocity

The expansion field is determined by solving a Poisson equation for  $\Phi^*$  [1],

$$\frac{1}{r^*} \frac{\partial}{\partial r^*} \left( r^* \frac{\partial \Phi^*}{\partial r^*} \right) + \frac{\partial^2 \Phi^*}{\partial z^{*2}} = Q^*(r^*, z^*). \quad (13)$$

A Gaussian heat release,  $Q^*(r^*, z^*)$ , is the assumed forcing function which is normalized such that

$$\int_0^\infty \int_0^\infty \int_0^\infty Q^*(r^*, z^*) r^* dr^* d\phi dz^* = 1. \quad (14)$$

The  $r^*$ -dependency of the Gaussian is weighted by the plume width  $R_o^*(1.32) = 0.417$ , i.e., at the top of the continuous flame zone. For  $z^* > 1.32$ ,  $Q^*(r^*, z^*)$  decays rapidly in the  $z^*$ -direction as shown in Eq. (15).

$$Q^*(r^*, z^*) = \begin{cases} \frac{1}{\pi R_o^{*2} [1.32 + 0.5\sqrt{\pi}]} e^{-5.76r^{*2}}, & z^* \leq 1.32 \\ \frac{1}{\pi R_o^{*2} [1.32 + 0.5\sqrt{\pi}]} e^{-5.76r^{*2} - z^{*2}}, & z^* > 1.32 \end{cases} \quad (15)$$

This not only helps to mimic the time-averaged behavior of the intermittent flame zone but also aids in the numerical computation of a smooth  $\Phi^*(r^*, z^*)$ . Figure 3 shows  $Q^*$  for a single fire throughout the computational domain,  $0 \leq r^* \leq 10$ ,  $0 \leq z^* \leq 20$ . The boundary condition along the centerline displays the symmetry of the potential in cylindrical coordinates and the one on the  $r^*$ -axis does not allow flow to cross it.

$$\begin{aligned} \frac{\partial \Phi^*}{\partial r^*}(0, z^*) &= 0 & \Phi^*(10, z^*) &= \Phi_a^*(10, z^*) \\ \frac{\partial \Phi^*}{\partial z^*}(r^*, 0) &= 0 & \Phi^*(r^*, 20) &= \Phi_a^*(r^*, 20) \end{aligned} \quad (16)$$

The boundary conditions subscripted by an "a" refer to the asymptotic value of  $\Phi^*$  which is simply the Green's function for a point source,

$$\Phi_a^*(r^*, z^*) = -\frac{(1-\chi)}{2\pi\sqrt{r^{*2} + z^{*2}}}. \quad (17)$$

For all calculations shown here  $\chi = 0.35$ . This asymptotic potential also supplies the expansion velocity field for  $r^* > 10$  and  $z^* > 20$ .

The solution to Eqs. (13 - 17) is shown in Fig. 4. The orientation of the surface is chosen in order to accentuate the most important features.  $\Phi^*$  is calculated using the separable elliptic Rayleigh-Ritz-Galerkin two dimensional partial differential equation solver *SERRG2* from the *TOMS* library [4, 5]. Forty six-point splines were used in the  $r^*$ -direction. Fifty were used in the  $z^*$ -direction. For consistency, this result was checked against those obtained from the centered finite difference solver *HWSCYL* and the staggered finite difference package *HSTCYL*, both from *FISHPACK*. For the *FISHPACK* solutions of  $\Phi_{ij}^*$ ,  $\Delta r^* = \Delta z^* = 5/64$  were used. The resulting velocities in the axial,  $w_z^*(r^*, z^*)$ , and radial,  $w_r^*(r^*, z^*)$ , directions are shown in

Figs. 5 a and 5 b, respectively. These velocities are small compared with the vorticity induced velocities. The numerical techniques used to compute the velocity from the potential will be discussed in a later section.

### Stokes Stream Function for the Vorticity Induced Velocity

The stream function is determined by solving a different Poisson equation,

$$r^* \frac{\partial}{\partial r^*} \left( \frac{1}{r^*} \frac{\partial \Psi^*}{\partial r^*} \right) + \frac{\partial^2 \Psi^*}{\partial z^{*2}} = -r^* \omega_\phi^* (r^*, z^*), \quad (18)$$

which has the vorticity  $\omega_\phi^* (r^*, z^*)$  as its inhomogeneity. The empirically determined profiles based on the centerline temperature,  $\Theta^* (z^*)$ , and vertical velocity,  $U_m^* (z^*)$ , are employed to determine  $\omega_\phi^*$  by taking the curl of the velocity obtained from this Gaussian model.

$$\omega_\phi^* (r^*, z^*) = \frac{2r^* U_m^* (z^*)}{R^{*2} (z^*)} e^{-\left(\frac{r^*}{R^* (z^*)}\right)^2} \quad (19)$$

The surface defined by this forcing function is shown in Fig 6. The boundary conditions for  $\Psi^*$  at the centerline and ground level make these axes streamlines, i.e., no flow may cross them. The other two, as with the potential, are based on the appropriate asymptotic behavior of  $\Psi^*$ ,

$$\begin{aligned} \Psi^* (0, z^*) &= \Psi^* (r^*, 0) = 0 \\ \Psi^* (10, z^*) &= \Psi_a^* (10, z^*); \Psi^* (r^*, 20) = \Psi_a^* (r^*, 20). \end{aligned} \quad (20)$$

The form of the asymptotic stream function,  $\Psi_a^*$ , is quite complex. It is convenient to first convert to a polar coordinate system  $(\xi, \theta)$ ,

$$\begin{aligned} \xi &= \sqrt{r^{*2} + z^{*2}}, & \theta &= \tan^{-1} \left( \frac{r^*}{z^*} \right), \\ \mu &= \cos \theta, & x &= \frac{1 + \mu}{2}. \end{aligned} \quad (21)$$

In order to determine the asymptotic stream function from Eq. (18), the vorticity is replaced by its asymptotic value,

$$\begin{aligned} \omega_\phi^* (r^*, z^*) &\sim \xi^{-4/3} \Omega (\theta) \text{ as } (\xi \rightarrow \infty), \\ \Omega (\mu) &= -\frac{6\pi A^2 B}{7(1-\chi) [\mu^{7/3}]} e^{\frac{3\pi AB}{7(1-\chi)} \left(1 - \frac{1}{\mu^2}\right)}. \end{aligned} \quad (22)$$

The form of the asymptotic stream function  $\Psi_a^* [1]$  is

$$\Psi_a^* (r^*, z^*) = \xi^{5/3} G (\theta). \quad (23)$$

Equations (21 - 23) are substituted into the Eqs. (18 - 20) to obtain a forced hypergeometric equation in  $G$  and  $x$  with homogeneous boundary conditions,

$$\frac{d^2 G}{dx^2} + \frac{10}{9x(1-x)} G = 4 \Omega (x), \quad G(0.5) = 0, \quad G(1) = 0. \quad (24)$$

The solution for  $G(x)$ , shown in Fig. 7, was obtained via numerically integrating Eq. (24) using the collocation boundary value problem solver *COLNEW* from *ODE* in the network library. Results were checked against those obtained by using the finite difference boundary value problem algorithms listed in Ref. [6].  $\Psi^*$  can now be determined numerically using the fourth order

*FISHPACK* routine *SEPX4*. The consistency is checked by calculating  $\Psi^*$  using the fourth order *FISHPACK* routine *SEPELI*. As for  $\Phi_{ij}^*$ ,  $\Delta r^* = \Delta z^* = 5/64$  were used as the step sizes. The surface  $\Psi^*(r^*, z^*)$  is given in Fig. 8 a. Quantitative streamlines, shown in Fig. 8 b, display the expected inflow towards the fire near the ground level and the subsequent strong flow up into the plume. The axial,  $v_z^*(r^*, z^*)$ , and radial,  $v_r^*(r^*, z^*)$ , vorticity-induced velocity components are shown in Figs. 9 a and 9 b, respectively. The numerical procedure used to determine them is discussed below.

### Single Fire Composite Velocity Field

The single fire velocity field,  $\mathbf{u}^*$ , consists of a solenoidal component,  $\mathbf{v}^*$ , and an irrotational component,  $\mathbf{w}^*$ , such that

$$\mathbf{u}^* = \mathbf{v}^* + \mathbf{w}^*. \quad (25)$$

In order to determine the radial velocity  $u_r^*$  and the axial velocity  $u_z^*$ , appropriate derivatives of the potential and stream function are taken and summed, as indicated in Eqs. (2 and 3), to give the complete flow field for a single fire. In practice, since  $\Phi_{ij}^*$  and  $\Psi_{ij}^*$  are discrete numerically determined approximations, a five-point finite difference scheme [6] is used to obtain the derivatives. The forward schemes, Eqs. (26 and 27), are used to determine the derivatives for small  $i$  or  $j$ . The backward schemes, used for large  $i$  or  $j$ , may be obtained by changing all the pluses in the indices to minuses and by taking the negative of  $\Delta r^*$  and  $\Delta z^*$ . Polynomial extrapolation [3] is used to determine the vorticity component of  $u_z^*$  at  $r^* = 0$ . The composite velocity  $\mathbf{u}$  is then known within the computational grid.

$$u_r^*(r_i^*, z_j^*) = \frac{-25\Phi_{i,j}^* + 48\Phi_{i+1,j}^* - 36\Phi_{i+2,j}^* + 16\Phi_{i+3,j}^* - 3\Phi_{i+4,j}^*}{12\Delta r^*} - \frac{1}{r_i^*} \frac{-25\Psi_{i,j}^* + 48\Psi_{i,j+1}^* - 36\Psi_{i,j+2}^* + 16\Psi_{i,j+3}^* - 3\Psi_{i,j+4}^*}{12\Delta z^*} \quad (26)$$

$$u_z^*(r_i^*, z_j^*) = \frac{-25\Phi_{i,j}^* + 48\Phi_{i,j+1}^* - 36\Phi_{i,j+2}^* + 16\Phi_{i,j+3}^* - 3\Phi_{i,j+4}^*}{12\Delta z^*} + \frac{1}{r_i^*} \frac{-25\Psi_{i,j}^* + 48\Psi_{i+1,j}^* - 36\Psi_{i+2,j}^* + 16\Psi_{i+3,j}^* - 3\Psi_{i+4,j}^*}{12\Delta r^*} \quad (27)$$

Fig. 10 a shows the vorticity,  $v_z^*$ , the expansion,  $w_z^*$ , the composite,  $u_z^*$ , and the empirical,  $U_m^*$ , velocities along the centerline. The agreement between the numerical composite and the empirical fit from Table I is excellent. The ground level vorticity,  $v_r^*$ , expansion,  $w_r^*$ , and composite,  $u_z^*$ , velocities are shown in Fig 10 b. These two comparisons agree well with Figs. 3 and 4, respectively, of Ref. [1].

Figure 11 shows the final result of this analysis. The surface for the dimensionless total axial velocity for a single fire,  $u_z^*$ , is shown in Fig 11 a. The axial velocity peaks on the centerline in the intermittent flame region and decays from the maximum slowly in  $z^*$  and rapidly in  $r^*$ . The surface for the dimensionless total radial velocity for a single fire,  $u_r^*(r^*, z^*)$ , is shown in Fig 14 c. This surface is more complex because the maxima for the expansion and solenoidal fields are of the same order but are of different signs. The largest radial velocities are near the fire and are directed towards it, as expected.

### Acknowledgments

This research is supported by US DOC NIST BFRL grant No 60NANB1D1168. A Graduate Fellowship was also received from the National Science Foundation.

### References

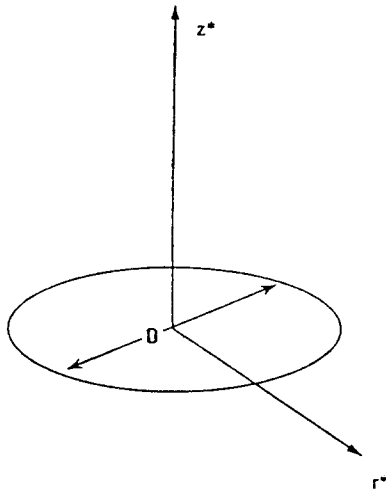
- [1] Baum, H.R., and McCaffrey, B.J., "Fire-Induced Flow Field - Theory and Experiment," *Fire Safety Science - Proceedings of the Second International Symposium*, New York: Hemisphere, 129 - 148, 1989.
- [2] McCaffrey, B.J., "Momentum Implications for Buoyant Diffusion Flames," *Combustion and Flame* 52, 149 - 167, 1986.

[3] Press, N.H., et al., *Numerical Recipes*, Cambridge, England: Cambridge University Press, 1989.

[4] Kaufman, L., and Warner, D.D., "High-Order, Fast-Direct Methods for Separable Elliptic Equations," *SIAM Journal of Numerical Analysis*, 21:4, 672 - 694, August, 1984.

[5] Kaufman, L., and Warner, D.D., "Algorithm 685: A Program for Solving Separable Elliptic Equations," *ACM Transactions on Mathematical Software*, 16:4, 325 - 351, December, 1990.

[6] Burden, R.L., and Faires, J.D., *Numerical Analysis*, 4<sup>th</sup> ed., Boston: PWS-Kent, 1989.



Axisymmetric cylindrical coordinate system with  $z^*$  positive upward and  $r^*$  centered on the heat source.

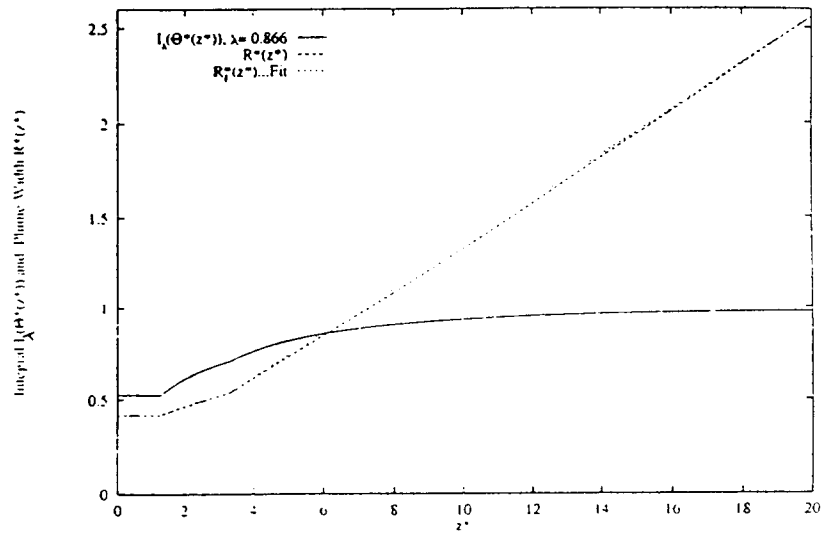
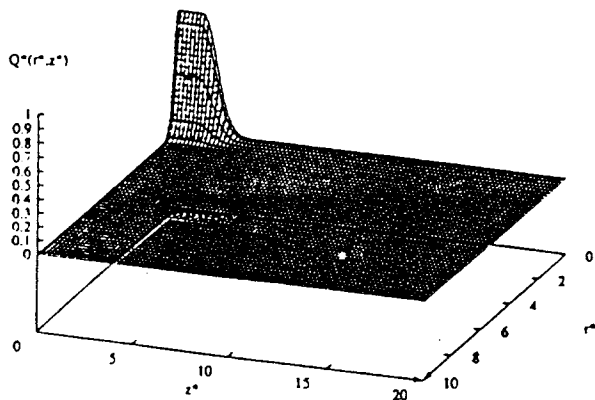


Fig. 2 The integral  $I_0(\Theta^*(z^*))$ , as obtained numerically from Eq. (8), the plume width  $R^*(z^*)$  from Eq. (10), and the fit  $R_T^*(z^*)$  based on Table I are plotted against  $z^*$ . The discontinuities in the slopes are direct consequences of the profiles defined in Table I.



3. Heat release source term  $Q^*(r^*, z^*)$  from Eq. (15). A right hand coordinate system is used exclusively throughout. All surface plots are oriented so as to highlight the most important regions. The arrows help eliminate any ambiguity. Shown on the  $(r^*, z^*)$ -plane is the corresponding contour. The lateral curvilinear lines on the surface indicate the level of the contour line was determined.

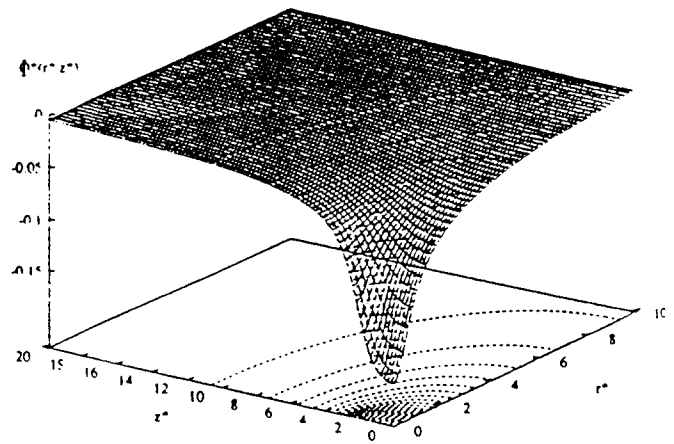


Fig. 4 Surface plot of the potential  $\Phi^*(r^*, z^*)$  as determined by solving Eqs. (13 - 17) with the *SERP2* package. 45 six-point splines were used in the  $r^*$ -direction while 55 six-point splines were used in the  $z^*$ -direction.

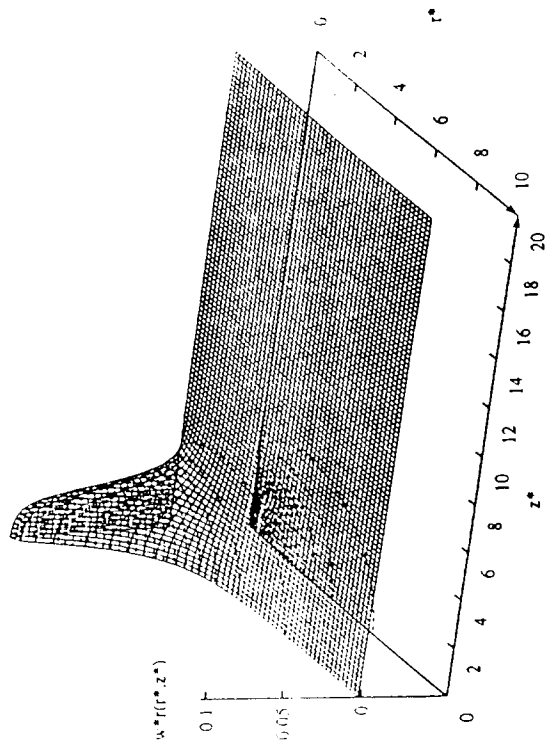


Fig. 5 b. Surface plot of the radial velocity due to expansion  $w_r(r^*, z^*)$ . Again, the local maximum is situated near the location of the fire.

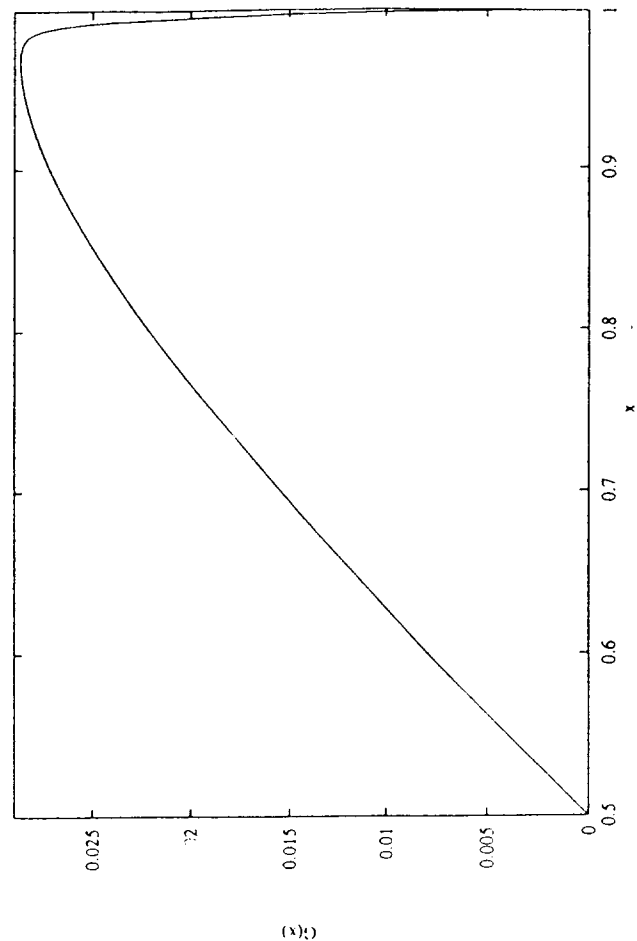


Fig. 7. The solution,  $G(x)$ , of the forced hypergeometric equation as determined by Eq. (24) via the COLNEW package.  $G(x)$  has a boundary layer near  $x = 1$ .

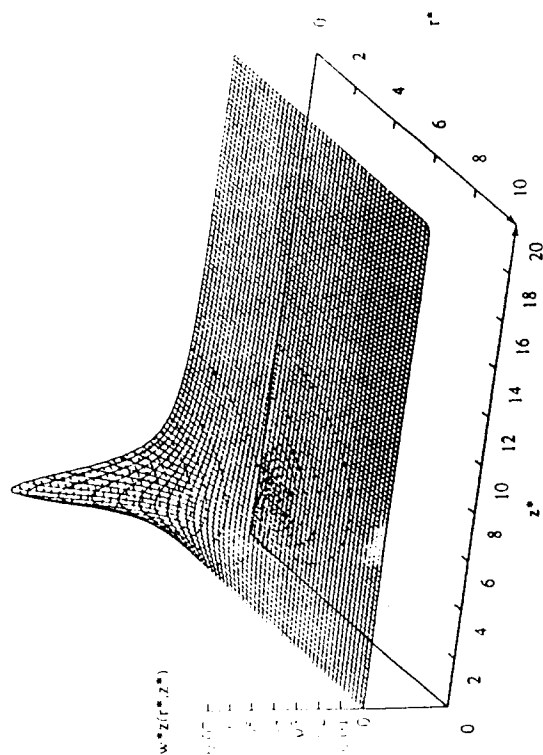


Fig. 5 a. Surface plot of the axial velocity due to expansion,  $w_z(r^*, z^*)$ , which was determined using the fourth order forward and backwards difference differentiation scheme shown in Eqs. (26 and 27).  $w_z(r^*, 0) = 0$ . The local maximum occurs on the centerline near the fire location.

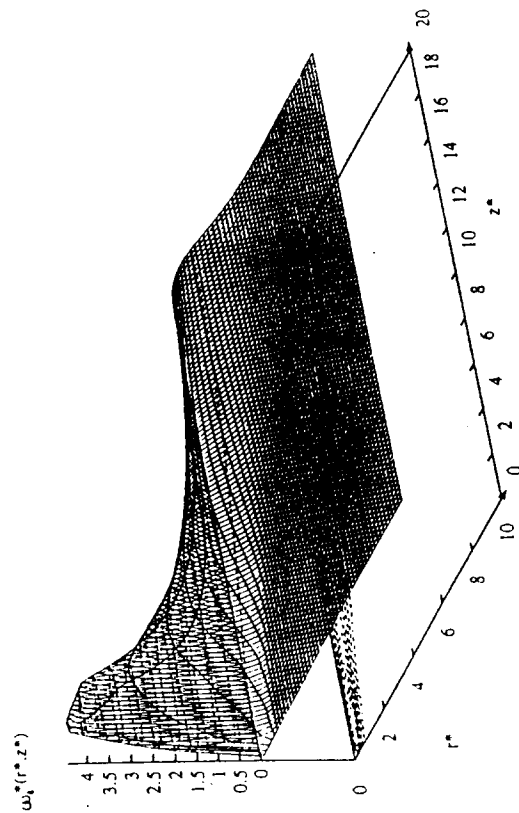


Fig. 6. Surface plot of the vorticity  $\omega_\theta(r^*, z^*)$ , from Eq. (19). Notice that the vorticity is greatest near the fire.

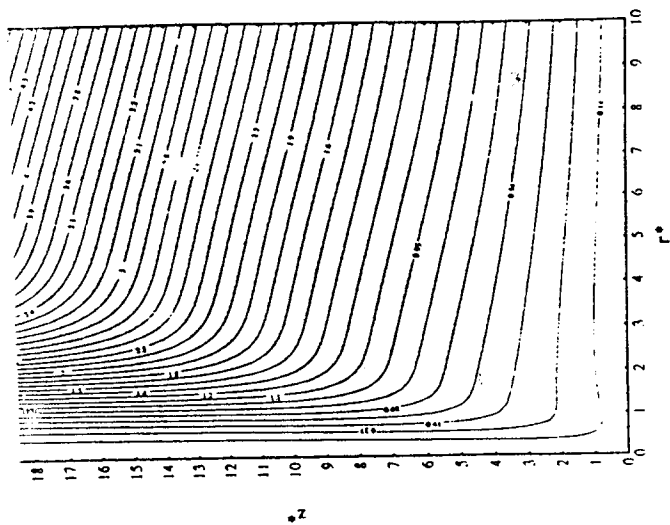


Fig. 8 a. Surface plot of the stream function  $\Psi^*(r^*, z^*)$  as determined by solving Eqs. (18-20) with the SEPXD package. It is fourth order accurate. The grid used has 128 points in the  $r^*$ -direction and 256 in the  $z^*$ -direction. The inflection at the boundary  $(r^*, 20)$  is responsible for causing stream lines to change from mostly radial to mostly axial flow.

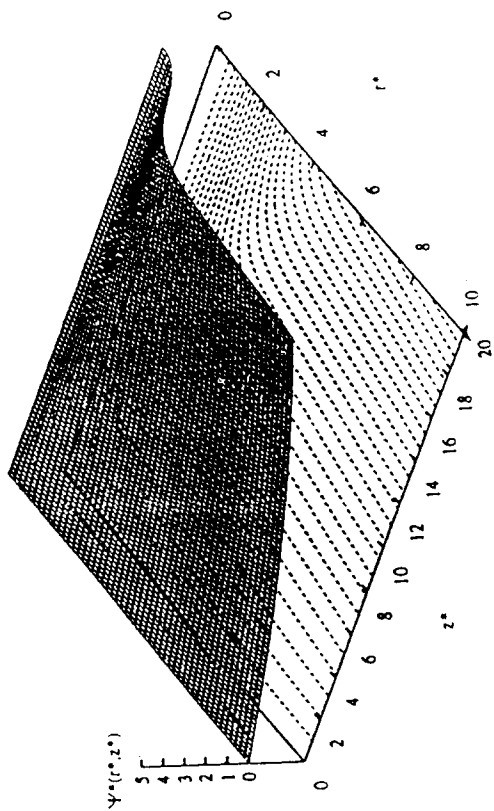


Fig. 8 b. Surface plot of the stream function  $\Psi^*(r^*, z^*)$  as determined by solving Eqs. (18-20) with the SEPXD package. It is fourth order accurate. The grid used has 128 points in the  $r^*$ -direction and 256 in the  $z^*$ -direction. The inflection at the boundary  $(r^*, 20)$  is responsible for causing stream lines to change from mostly radial to mostly axial flow.

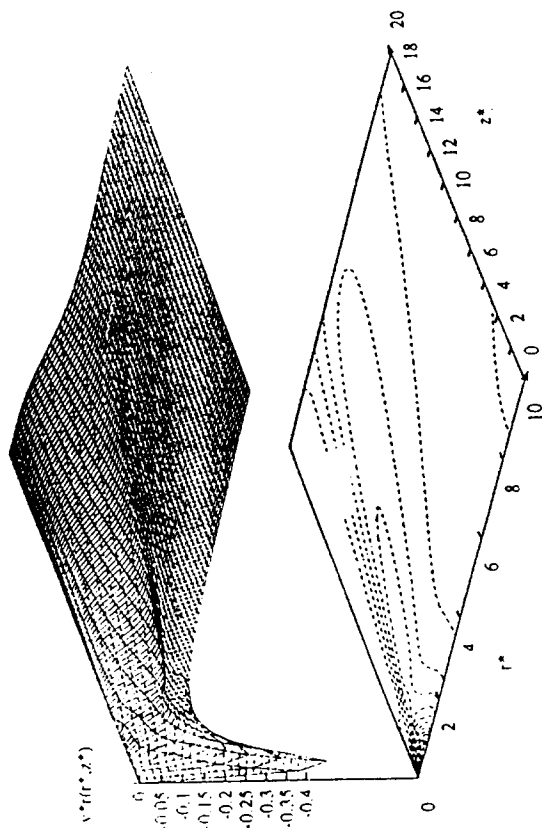


Fig. 9 a. Surface plot of the axial velocity due to vorticity  $v_z^*(r^*, z^*)$  determined using the fourth order forward and backward difference differentiation scheme in Eqs. (26 and 27). The maximum velocities occur on the centerline, decaying as  $r^*$  increases. The  $r^*$  range increases as  $z^*$  increases. Comparison with Fig. 5 shows that  $\max\{v_z^*(r^*, z^*)\} \gg \max\{v_r^*(r^*, z^*)\}$ , i.e., the vorticity dominates the radial velocity.

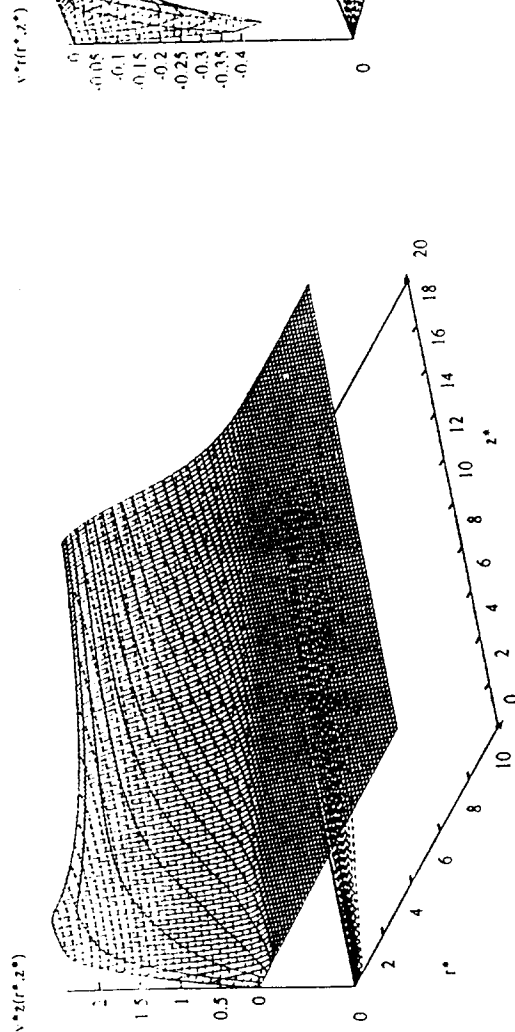


Fig. 9 b. Surface plot of the radial velocity due to vorticity  $v_r^*(r^*, z^*)$  determined using the fourth order forward and backward difference differentiation scheme in Eqs. (26 and 27). The maximum velocities occur on the centerline, decaying as  $r^*$  increases. The  $r^*$  range increases as  $z^*$  increases. Comparison with Fig. 5 shows that  $\max\{v_r^*(r^*, z^*)\} \gg \max\{v_z^*(r^*, z^*)\}$ , i.e., the vorticity dominates the radial velocity.



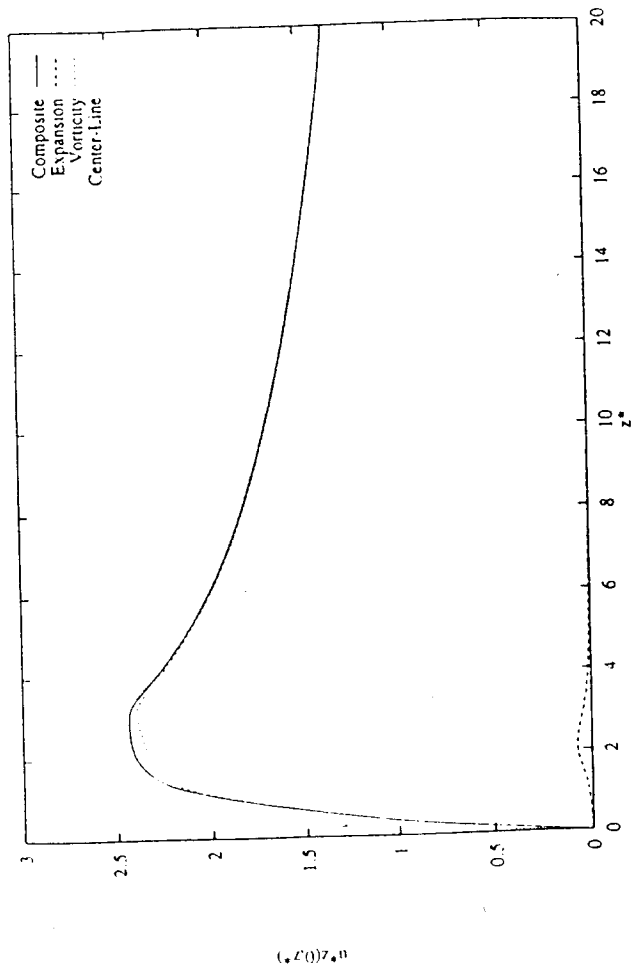


Fig 10 a. Centerline axial velocities which may be compared with Fig. 3 of Ref [1]. There is good agreement between the empirical velocity and the numerically determined composite

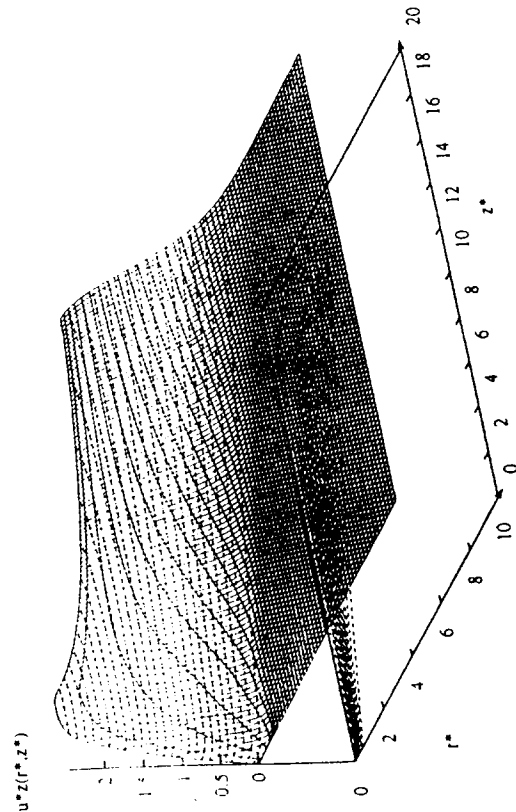


Fig 11 a. Surface plot of the composite axial velocity  $u_z(r, z)$ . The maximum velocities occur, as expected, near the centerline

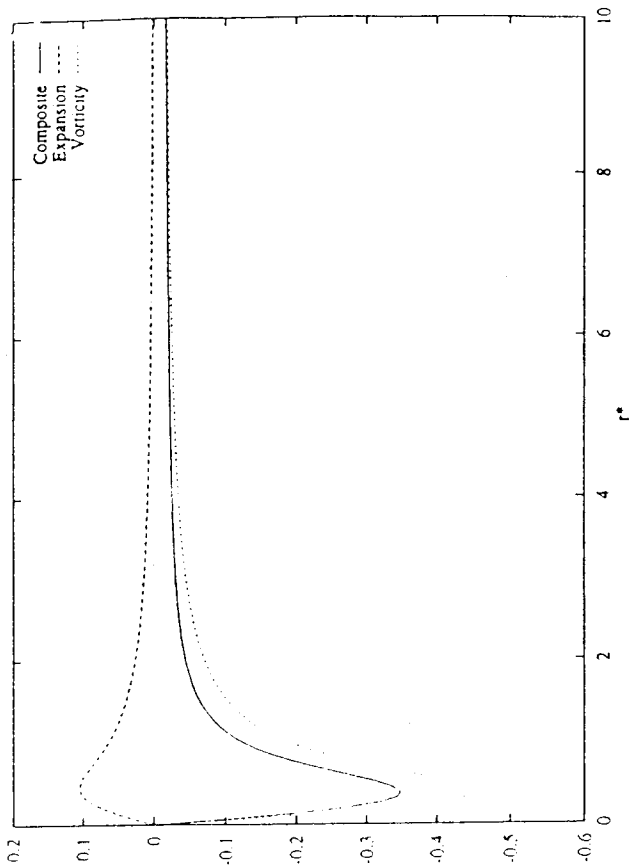


Fig 10 b. Ground level radial velocities which show good agreement with Fig. 4 of Ref [1].

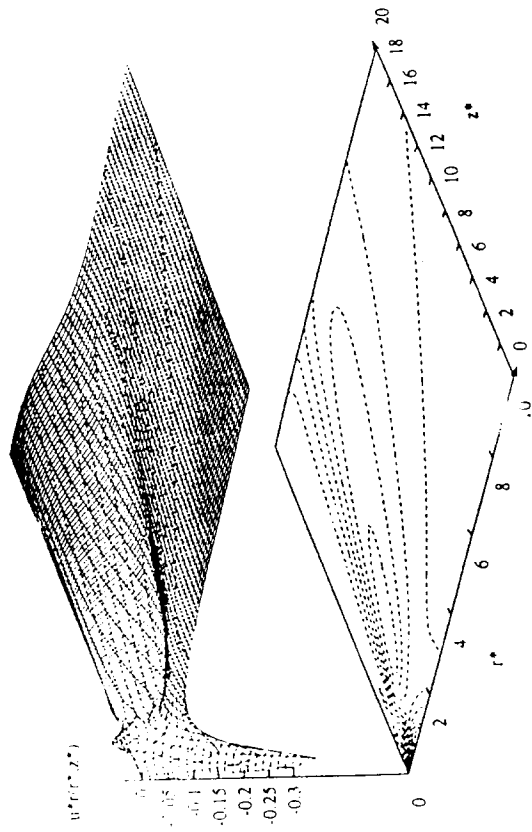


Fig 11 b. Surface plot of the composite radial velocity  $u_r(r, z)$ . The local maximum in  $u_r(r, z)$  is responsible for the complicated character of the surface just above the strong inflow.